Experimental Thermal and Fluid Science 139 (2022) 110725

Contents lists available at ScienceDirect

Experimental Thermal and Fluid Science

journal homepage: www.elsevier.com/locate/etfs

Spray trajectory and 3D droplets distribution of liquid jet in crossflow with digital inline holography

Lei Wang, Letian Zhang, Wenhui Lin, Yingchun Wu *, Xuecheng Wu

State Key Laboratory of Clean Energy Utilization, Zhejiang University, Hangzhou, 310027, China

ARTICLE INFO

Keywords:
Primary breakup
Crossflow spray
Digital holography
Jet trajectory
Size distribution

ABSTRACT

Liquid jet in crossflow (LJCF) has a wide application in the actual engine engineering. This article presents an experimental investigation of a water jet transversely injected into a subsonic crossflow through digital inline holographic imaging, and presents the relationship between the column trajectory and the downstream droplet distribution. A phenomenological analysis based on high-speed digital inline holography (DIH) with the frequency of 25 kHz is presented to interpret the source of droplets with different sizes in the bag breakup mode and the shear breakup mode. High-resolution DIH with a spatial resolution of 5.5 μ m is applied to measure breakup point, droplet size, and location under 30 mm downstream of the orifice. The experiment is carried out under normal temperature and pressure. Gas Weber number We_g varies from 11 to 67, and the liquid to gas momentum ratio q changes from 10 to 28, which are mainly under bag breakup and multi-mode breakup regime. Crossflow velocity profiles are also measured. Liquid penetration were obtained and fitted through spray pattern under $x/d_j < 10$ and through downstream droplet statistics under $12 < x/d_j < 70$ separately. Under the cases studied, spray penetration evaluated by droplet statistics is larger than that evaluated through spray pattern. In addition, droplet size is relative large in the core region of the spray under higher We_g, possibly due to the presence of vortices in the core region and stronger aerodynamic effects at the periphery of spray. This research presents the quantification of the primary breakup process and corresponding three-dimensional (3D) downstream SMD distribution simultaneously, which helps improve the understanding of spray evolution in crossflow.

1. Introduction

Liquid jets in crossflow (LJCF) widely exist in the afterburner of aero engines and scramjet engines. The spray characteristics, such as droplet size and velocity distributions, have a direct impact on the combustion stability, efficiency and pollutant emission in the combustion chamber. Therefore, it is of significance to investigate the process of liquid jet atomization in crossflow comprehensively to optimize the operating conditions and the designs of the combustors. Under the interaction of aerodynamic force, surface tension, viscous force, and internal turbulence, the jet liquid column breaks apart into liquid ligaments, liquid lumps and droplets of different sizes [1]. Those ligaments and droplets are further broken to form smaller droplets under the shear force of crossflow, which is called secondary breakup [2]. The mechanisms of liquid jets in crossflow show great differences and strong regularity under different working conditions [3]. Early studies [4,5] mainly focused on spray penetration, jet trajectories that were observed repeatedly. Soo-Young No [6] and Wang [7] reviewed the empirical correlations for the jet trajectory and breakup length in uniform crossflow, and various nondimensional trajectory fitting formulas for different LJCF conditions were also proposed in recent years [8–10]. The fitting formula explored the effects of We_g, q, Re, and physical properties of the liquid, yet discrepancies between the predicted curves exist even for the correlations with the same functional form. The trajectory difference observed among different studies could attribute to measurement methods, the liquid jet boundary definition, nozzle geometry, boundary layer of the incoming jet and gas flows, and so on. Unfortunately, the incoming velocity profiles are rarely reported, and insufficient resolution imaging techniques may result in under-predicting the trajectory curve [11]. In recent years, researchers [10–12] have discussed the influence of nozzle geometry parameters on jet tracking. A unified form for the formula has not been established already.

Besides jet penetration, the primary breakup mechanism is also of interest with the development of high-speed measurement techniques. Wu [5] reported four breakup types of nonturbulent liquid jet with shadowgraphy and distinguished breakup regime maps with the Weber

* Corresponding author.
E-mail address: wuyingchun@zju.edu.cn (Y. Wu).

https://doi.org/10.1016/j.expthermflusci.2022.110725
Received 11 September 2021; Received in revised form 14 June 2022; Accepted 23 June 2022
Available online 3 July 2022

Nomenclature

C_D	Drag coefficient
d_o	Orifice exit diameter
d_j	Liquid jet diameter
q	Liquid to air momentum flux ratio ($\rho_l u_j^2/\rho_g u_g^2$)
Re	Reynolds number
u	Velocity
We_g	Aerodynamic Weber number ($\rho_g u_g^2 d_j/\sigma$)
x, y, z	Coordinates of the jet spray

Subscripts

b	Breakup
g	Gas
j	Jet
o	Orifice

Greeks

δ	Boundary layer thickness
ρ	Density
σ	Liquid surface tension
μ	Dynamic viscosity
Γ	Reconstructed complex amplitude from hologram

number and the momentum flux ratio, which are capillary, bag, multi-mode, and shear breakup regime. Sallam [13] studied the boundary for the transition between the bag breakup regime and the multi-mode breakup regime with pulsed shadowgraphy and holography. Wu [14] found that the droplet size distribution was affected by q in the x/d_j = 150 and 200 downstream. Ng [15] focused on the study of droplet formation and reported the sizes and velocities of node droplet, ring droplet, and bag droplets in the bag breakup process with the Weber number lower within 30. A large number of attempts were also made to study the relationship between the droplet distribution and the operating condition in LJCF. Inamura [16] measured the droplet size and velocity distribution of atomized droplets in the field within 280 mm downstream, with the jet diameters of 1 mm and 2 mm separately. When the velocity of crossflow got higher, the droplet size in the core area was larger, and the size distribution of the spray field became more uniform as the large droplets failed to reach the top field. Lubarsky [17,18] studied the effect of Weber number on the droplet size with phase Doppler particle analyzer (PDPA) under ambient temperature and pressure, the x/d_j=66 and q was kept constant. The droplet size distribution is found to be bimodal when We_g = 33, the drop size results show an increase with the penetration depth under We_g of 133~2020. The formation of droplet distribution under low We_g need to be further studied and analyzed. Based on the experimental statistics, several fitting formulas for the Sauter mean diameter (SMD) of the droplets were proposed. Kihm [19] obtained the normalized SMD fitting formula based on Buckingham π theorem for cross-injecting sprays through Malvern system. Song [20] also researched SMD expression with PDPA and spray trajectory with Mie scattering of LJCF at elevated pressure. Due to the measuring principle of optical method like PDPA, the irregular droplets during early atomization and the dynamic atomization process in the transition region limits the applications.

M. Broumand [3] provided a comprehensive review on the research progress of liquid jet in a subsonic gaseous crossflow. It is recognized that droplets may originate from the liquid column, bag membrane, ligament rings and nodes. These droplets show great differences in the spatial, size, and velocity distribution. The spatial and velocity distribution of the downstream droplets are related to the jet trajectory and primary breakup process, and furthermore, are related to the nondimensional number such as We_g, q, Re and so on. The relationship between the upstream characteristics and downstream size distribution relies on further quantitative analysis.

Digital inline holography (DIH) is a three-dimensional imaging measurement method based on the principle of coherent interference, which can realize the full field three-dimensional measurement of particle size and spatial distribution of atomized droplets [21–23], as well as vortex flows [24]. Our previous research [25] also shows the potentiality of digital holography to capture the atomization process and droplets field in spray. Guildenbecher [23] and Yao [26,27] used DIH to obtained the dynamic bag breakup process of a single droplet, including the size, spatial distribution and velocity distribution of secondary droplets. Olinger [28] also studied the near field structures of liquid jet in crossflow using double pulsed inline holographic system, results showed that there were a lot of non-spherical droplets. A correlation for the SMD under different crossflow Mach numbers and gas-to-liquid ratios was calculated. The SMD of the atomized droplets is mainly affected by the gas-to-liquid ratio of the nozzle and the Mach number of crossflow.

The objective of this study is to extend the understanding of the spray formation process by observing the breakup of a uniform round liquid jet in crossflow. Specifically, this study measures the jet trajectory, the column breakup location, and corresponding three-dimensional (3D) droplet distribution below x/d_j = 80. Velocity profiles of incoming air-flow and liquid jet diameter are measured in advance to provide more comprehensive information of experiments. Two picosecond pulsed digital inline holographic systems are built to obtain the aforementioned parameters simultaneously and study the atomization process of a liquid jet in crossflow at the near-nozzle region. The high-speed holographic system has a frequency of 25 kHz and is used to provide the time-resolved phenomenological information of the primary breakup of the liquid jet. The spatial SMD distribution of the atomized droplets, as well as the upstream jet trajectory, is statistically counted and analyzed using a high-resolution holographic system with an equivalent pixel size of 5.5 μm and field of view (FOV) of over 22 mm × 34 mm. Finally, phenomenological analyses and empirical formulas are proposed to help interpret the droplet size distribution under investigated cases.

2. Experimental setup

Fig. 1 shows the schematic diagram of the experimental system, which was comprised of an LJCF system and a holographic imaging system. The main body of the LJCF system was a 360 mm-long passage with an internal cross-section of 40 mm × 50 mm. as shown in Fig. 1(a). The beginning 210 mm of the passage was used to measure the air parameters and ensure a stable airflow. A pair of acrylic plate windows were mounted on the rest of the passage for holography. The atomizing airflow used in the experiments was provided by a three-phase high-pressure fan, which was connected to a frequency converter. The airflow passed through a 50 mm-long honeycomb with regular hexagons of 1.718 mm inside and then contracted into the passage to atomize the liquid jet. The air-flow velocity can be controlled by changing the electricity frequency with the frequency converter and its amplitude was measured with a pitot tube with a differential pressure transmitter, which was calibrated by a Lavision particle image velocimetry (PIV) system ahead of the experiments with the particle tracer of DEHS, as depicted in Fig. 1(c). During setup, the observed RMS velocity of the incoming air was found to be about 4.5% of the mean velocity, and the boundary layer thickness δ on the plate with the injection orifice was found to be about 4 mm~6 mm across. The influence of the boundary layer of crossflow to the liquid column was observed and discussed in the following section. The incoming airflow

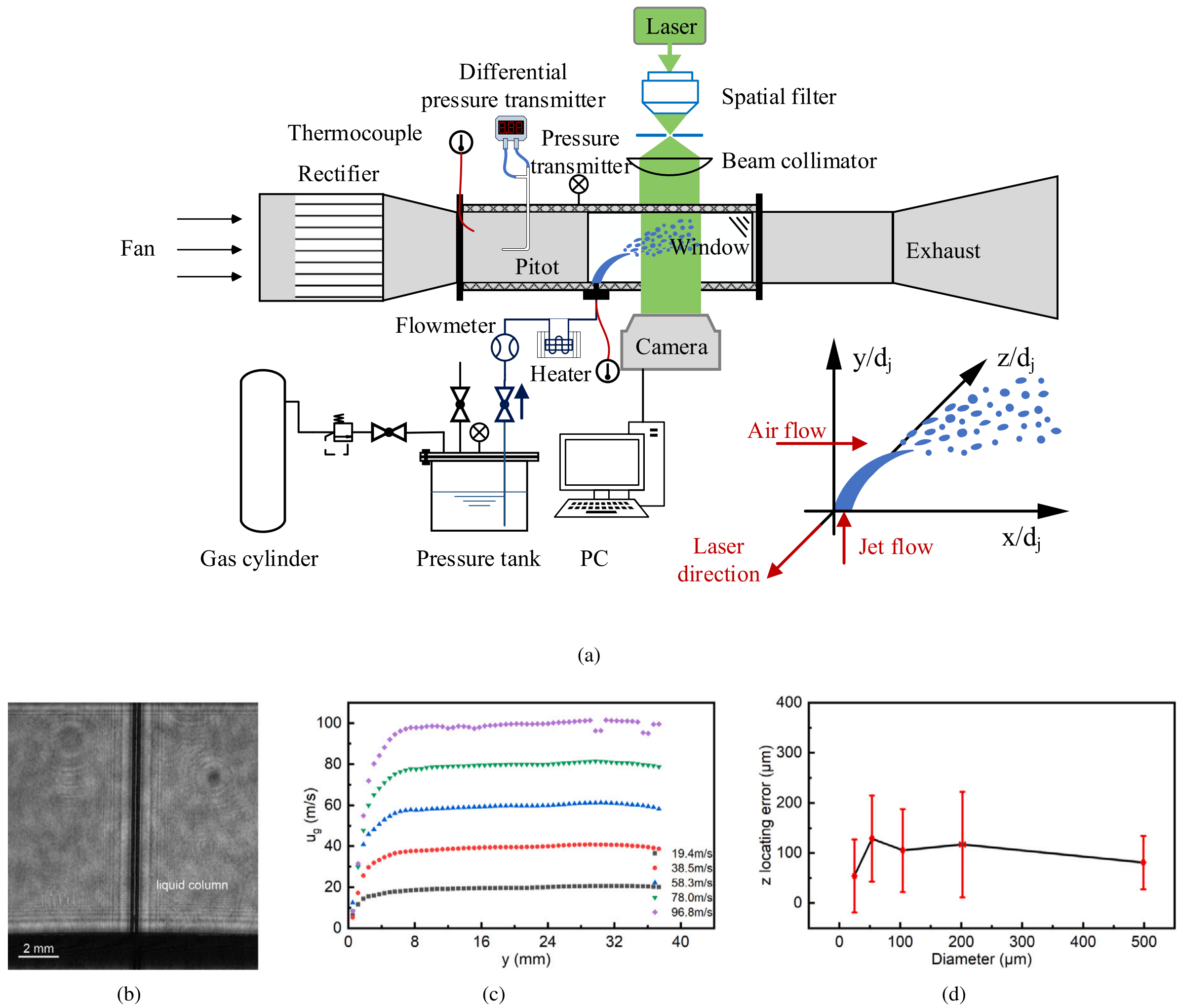

Fig. 1. Experimental set up of liquid jet in crossflow measurement with pulsed digital inline holographic system. (a) Schematic diagram of experiment system. (b) Jet flow diagram in still air. (c) Velocity profiles of incoming crossflow. (d) z locating error of high resolution holography using standard calibrator.

velocity profiles were uniform and stable in the region where the liquid column broke. A thermal couple and an absolute pressure gauge were also mounted along the passage to measure the air-flow temperature and absolute pressure, which can be used to calculate the density of the air.

Deionized water was injected transversely into the airflow by a nozzle and a liquid chamber. The liquid chamber was filled with deionized water and pressurized by gas from a compressed air tank. Driven by the gas pressure, water inside the chamber was forced through the nozzle and formed a liquid column transverse to the airflow. Detailed information of the nozzle installed in the passage can be found in the illustration in Fig. 1(a). Water was forced through a 0.5 mm circle hole on a 0.2 mm-thick metal plate, which was 3 mm below the internal wall of the passage. The fluid jet diameter of the outcoming liquid in still air was measured with a high-resolution camera and found to be uniform, as depicted in Fig. 1(b). A volume flow meter was installed upstream of the nozzle to measure the volume flow rate of the water, which was converted to the jet velocity by the jet diameter. The measuring range and accuracy of the aforementioned measurement instruments are listed in Table 1.

The structure of the jet and the mechanism of downstream droplets were studied by pulsed laser digital inline holography. The laser source used here has a wavelength of 532 nm and a pulse duration of under 1 ns. The equivalent pixel size of the system is 5.5 μm, and the spatial resolution is 6576 × 4384, providing a 36.168 mm × 24.112 mm field of view. The high-resolution camera synchronized with laser thorough a synchronizer, with a frequency of 2 Hz. To avoid the environmental light effect, the experiments were conducted in a dark room. The optical system was calibrated by a standard dot calibrator with dot size of 25 μm, 50 μm, 100 μm, 200 μm and 500 μm separately, as is shown in Fig. 1(d). The corresponding measurement size was 24.9 μm, 53.8 μm, 104.1 and 201.9 μm, and 498.6 μm, with standard deviation of 2.0 μm, 1.7 μm, and 1.5 μm, 3.9 μm, and 1.4 μm. The depth position measurement error was obtained by taking 8 different holograms, for each standard dot, the z locating error was calculated and evaluated, the average depth location errors for different dots range from 54 μm to 129 μm. Considering the computing efficiency, the z reconstructed interval for experimental data was set to be 0.1 mm. Table 2 listed the experimental conditions of cases used in this study. Those cases are tested to investigate the influence of two parameters on the atomization results, namely We_g and q, which get the most attention.

Table 1
Properties of instruments.

Instruments	Scale range	Test accuracy
Differential pressure transmitter	0~10 kPa	0.1%
Thermal couple	0~100 K	0.1 K
Volume flow meter	10~800 ml/min	1%

Table 2
Test conditions.

Case	U_j m s^{-1}	U_g m s^{-1}	We_g	q	d_j mm
Case 1	4.7	42.4	11.3	10.7	0.39
Case 2	6.7	42.8	11.0	21.3	0.38
Case 3	6.8	58.8	21.8	11.7	0.39
Case 4	8.9	82.0	36.5	10.5	0.35
Case 5	10.4	82.4	36.4	14.1	0.35
Case 6	12.3	82.6	41.0	19.8	0.39
Case 7	12.8	72.1	30.5	28.2	0.38
Case 8	12.8	108.4	67.0	13.0	0.38
Case 9	14.2	88.6	42.4	22.9	0.35

3. Data processing

In order to retrieve droplets' size and three-dimensional location, holograms need to be handled with a reconstruction algorithm and droplet detection algorithm. In this work, an angular spectral method was applied to reconstruct the holograms

$$\Gamma\left(x,y;z_{\mathrm{r}}\right)=\mathcal{F}^{-1}\left\{\mathcal{F}[R\cdot h(m,n)]\times\exp\left[-\mathrm{i}\frac{2\pi z_r}{\lambda}\sqrt{1-\left(\frac{\lambda m}{\mathrm{M}\Delta\mathrm{x}}\right)^2-\left(\frac{\lambda n}{\mathrm{N}\Delta\mathrm{y}}\right)^2}\right]\right\}, \tag{1}$$

where $\Gamma\left(x,y;z_{\mathrm{r}}\right)$ denotes the reconstructed complex amplitude at distance z_{r} from the hologram, R is the reference wave which can be simplified to the unit amplitude for inline holography, (m,n) and (x,y) label pixels on the hologram and the reconstructed slice image, $\mathcal{F}$ and $\mathcal{F}^{-1}$ represent the Fourier transform and inverse Fourier transform. Only a few droplets are focused on the slice at z_{r}. For high resolution holograms with equivalent pixel size of 5.5 μm and spatial resolution of 6576 × 4384, a series of slices between z_{r} = 280 mm and z_{r} = 318 mm with an interval of 0.1 mm were reconstructed. For high speed holograms with the frame rate of 25 kHz, equivalent pixel size of 15.3 μm and spatial resolution of 1280 × 800, the range of reconstructed slice is between 190 mm and 230 mm, with interval of 0.1 mm. Those reconstructed slices were treated with a wavelet base image fusion algorithm to yield an extended focus image (EFI) with all droplets in focused [29]. A hybrid method algorithm was adopted to detect the focused droplets and their spatial locations afterwards. For each droplet, the focus metric curve (FMC) was calculated through the variance of its edge gradient

$$\mathrm{FMC}(z_r)=\sum_n\sum_m\left\{\mathrm{Sobel}\ [I(x,y;z_r)]-\overline{\mathrm{Sobel}\ [I(x,y,z_r)]}\right\}^2, \tag{2}$$

where $I(x,y;z_r)=\left|\Gamma\left(x,y;z_r\right)\right|$, and Sobel operation is used to calculate the horizontal and vertical gradient magnitude of the image. The droplet size and 3D position were then determined at the focused slice to obtain more accurate results, which is the z_r position of the maximum value of FMC(z_r). Details of the algorithm can be found in previous works [29]. The droplet size accuracy of this system was calibrated by a standard calibrator. To eliminate spurious droplets caused by noises, droplets occupying more than four pixels were retained, resulting in the system's minimum detected droplet diameter, 12.4 μm.

In this paper, the water jet diameter d_j for each case was defined as the average diameter that just entered the crossflow region, which is 3 mm from the exit orifice of the metal, and was measured through a high-resolution camera in advance and was used to obtain the nondimensional values of x/d_j and y/d_j. The nozzle exit velocity v_{j} was measured by measuring the volume flow rate Q_{j} of injected test liquid, and was implemented by $v_{\mathrm{j}}=4Q_{\mathrm{j}}/(\pi d_j^2)$. The 3D locations of the identified droplets were further normalized with the jet diameter and their coordinate origin was shifted to the liquid jet location. The coordinate diagram in the upper left corner of Fig. 1(a) shows the definition of axis direction used in this study.

4. Results and discussions

4.1. The column trajectory

The digital inline hologram, reconstructed slice, corresponding 3D droplet field, and time-average image of a typical round nonturbulent liquid jet in crossflow are shown in Fig. 2. The focused and defocused droplets can be seen at the reconstructed slice in Fig. 2(b). The position of those droplets can be achieved through the aforementioned method, and the 3D droplet field from the hologram can be obtained, as shown in Fig. 2(d). The dot size represents the size of the droplet, and the color indicated the ratio of the short and long axes of the projection of every identified droplet, which is $\mathrm{L_{min}}/\mathrm{L_{max}}$. To distinguish the ligaments from the droplets, the value was limited between 0.33 and 1 in this study.

50 different EFIs of each case were selected to calculate the time-average jet pattern, as depicted in Fig. 2(c). To avoid the influence of uneven background light intensity, the binary image was obtained through an adaptive binarization processing method as follow

$$\text{threshold } = \min\left(th_1, 0.8th_2, 0.4\right), \tag{3}$$

where $th_2=\frac{\sum_{(p,q)\in D}\mathrm{I}_D(p,q)}{N_D}$ is the average gray value of a block region D, and $th_1=\frac{\min[\mathrm{I}_D(p,q)]+th_2}{2}$. Afterwards, the nondimensional trajectory under different cases can be obtained and fitted, as is shown in Fig. 3.

Comparing the case 4, 5, 6, and 7 in Fig. 3(a), the results suggest that the increase of q leads to higher penetration length under basically the same We, which is well known and analyzed in literatures [5,13]. Comparing the case 2 and 9, it can be found that the We_g number also has a negative effect on the penetration depth of the liquid column when the q is similar to each other. According to Wu [14] and Ng [15], the column trajectory can be approximated as $y/d_j=\sqrt{(\pi/C_D)\cdot(x/d_j)\cdot q}$ based on the aerodynamic force analysis a liquid jet element, where C_D is the drag coefficient. The Re_g increases with We_g, and thus leads to the larger C_D [30], resulting in a stronger bending of the liquid column trajectory. The jet diameters of liquid columns under different cases were found to change slightly, which were considered when determining the We_g and q. To take the jet diameter parameter into account, a dimensionless coefficient d_j/d_o is introduced in the fitting formula, where d_o is the nozzle exit diameter, which is 0.5 mm in this study. The new fitting formula shows better consistency with the experimental results compared with the original one. The fitting formula characterizes the relationship between the nozzle exit diameter and the jet diameter dimensionless.

$$\frac{y}{d_j}=1.846q^{0.351}We_g^{-0.055}\ln\left[1+1.908\left(\frac{x}{d_j}\right)\right], R^2=0.94, \mathrm{RSME}=0.75, \tag{4}$$

$$\frac{y}{d_j}=2.878q^{0.340}We_g^{0.012}\left(\frac{x}{d_j}\right)^{0.465}\left(\frac{d_j}{d_0}\right)^{1.883}, R^2=0.98, \mathrm{RSME}=0.30, \tag{5}$$

the curvature of the liquid column near the field changes with We_g. In the fitting formula, the We_g index is relatively small, which indicates that the jet penetration depth has a weak relationship with the We_g number after considering the liquid column breakup area. This formula is valid under the range of $0<x/d_j<10, 10<q<28, 10<We_g<67$.

4.2. The column breakup process

Fig. 4 shows the time-resolved liquid column breakup regime under different typical We_g numbers. The patterns were the reconstructed slices of high speed hologram under z_r = 208 mm. The $t^*=(\frac{\rho_j}{\rho_g})^{0.5}d_j/u_g$ is the characteristic time proposed by Ranger and Nicholls [31]. The

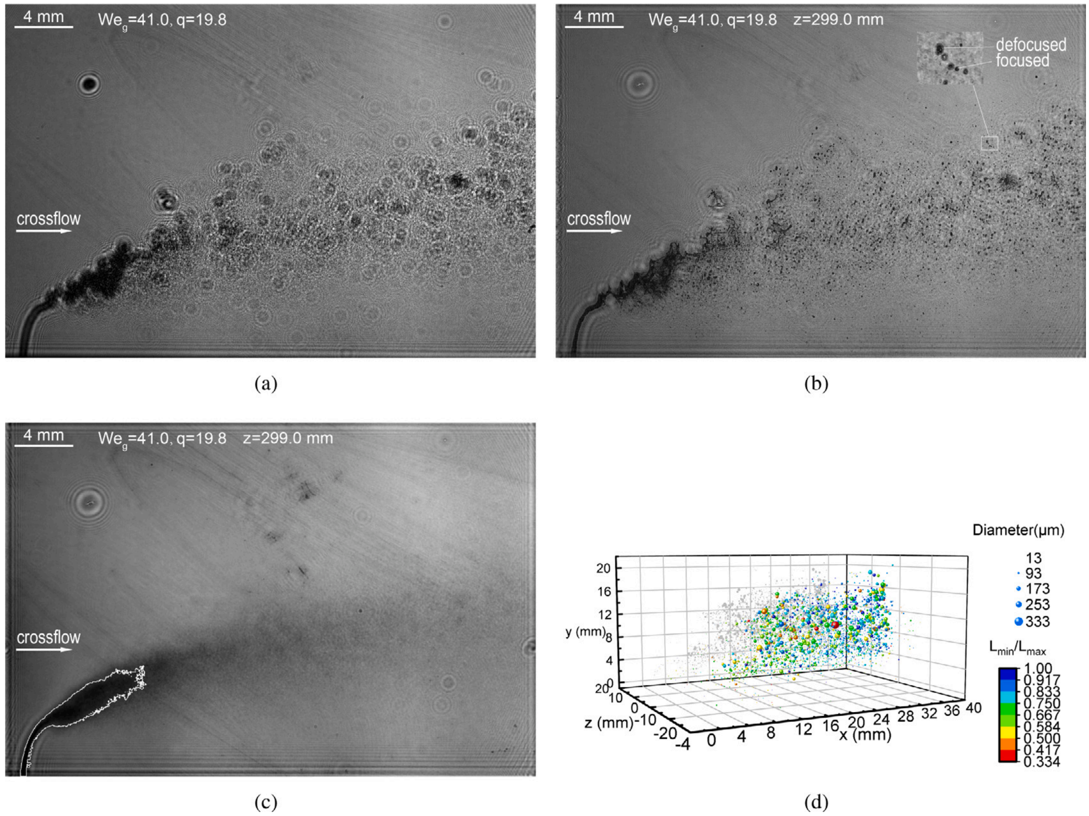

Fig. 2. Reconstructed image and detected droplets of a typical digital inline hologram of LJCF. $We_g = 41.0, q = 19.8$. (a) Hologram. (b) Corresponding reconstructed slice at $z = 299$ mm of hologram. (c) Time average reconstructed image and detected near field jet trajectory. (d) 3D droplet field.

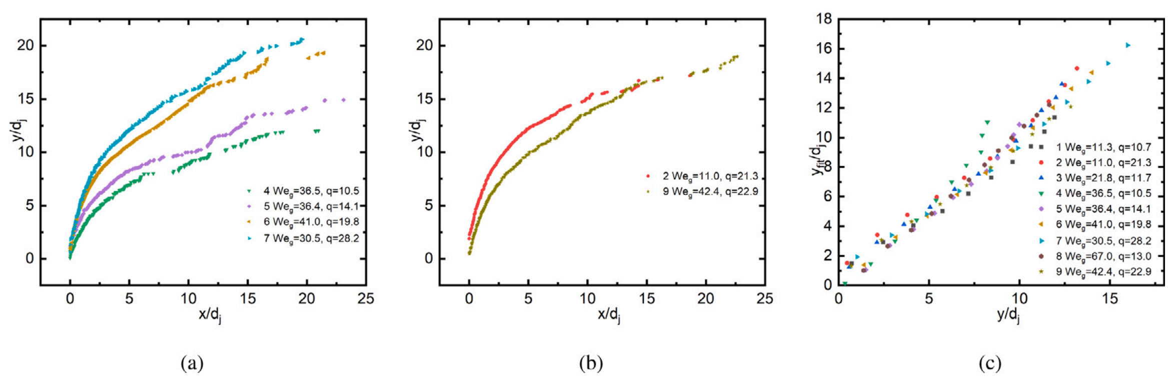

Fig. 3. Near field trajectory of LJCF. (a) Comparison of trajectories under different q. (b) Comparison of trajectories under different We_g. (c) Comparison of measurement jet penetrations and fitted results.

liquid column is blent and deformed due to the momentum exchange with the gas flow on the upstream side. Column waves form on the liquid column due to Rayleigh–Taylor instability, leading to troughs and knots appearing in succession. The trough is blown into a bag-like structure anchored to the knots, afterwards, the bag breaks up due to the higher pressure produced by the stagnating gas on the upwind side than on its downstream side, resulting in a shower of fine droplets downstream of the bag.

Under lower We_g, as depicted in Fig. 4(a), the knot, along with the strings formed by the contraction of liquid when the bag breaks up, keeps moving downstream and splits into droplets with various sizes. The bag breakup process takes about $2.3t^*$. As We_g rises to 36.4 or higher, a stronger drag force is exerted on the liquid column. The breakup time for bag is shorter and within $1.13t^*$ in Fig. 4(b). Before the liquid column is completely broken, sheared breakup process can be observed on the column, and the bag breaking process can still be observed at the end of the mixed liquid column, which indicates the coexistence state of shear breakup and bag breakup process. The videos of cases in the attachments can also prove the discussion presented here.

Fig. 4(c) shows the SMD distribution and mean transverse velocity distribution of the droplets in case 2, and Fig. 4(d) represents the corresponding results of the droplets in case 6. The area under calculation includes $5 < x/d_j < 43$, $0 < y/d_j < 27$, with the spatial resolution of $2d_j \times 2d_j$, the results are obtained through 1000 consecutive high speed holograms with sampling frequency of 25 kHz. The particle tracking algorithm (PTV) applied here can refer to [29]. The mean transverse velocity $\overline{u_y}$ is calculated by $\overline{u_y} = \sum d^3 u_y / \sum d^3$. The red lines in the figures represent the streamlines. Note that due to the limitation of the equivalent pixel size of high speed hologram, only dispersed droplets larger than 30 μm are counted. The transverse velocity distribution suggests that there exist negative v value in the downstream of the

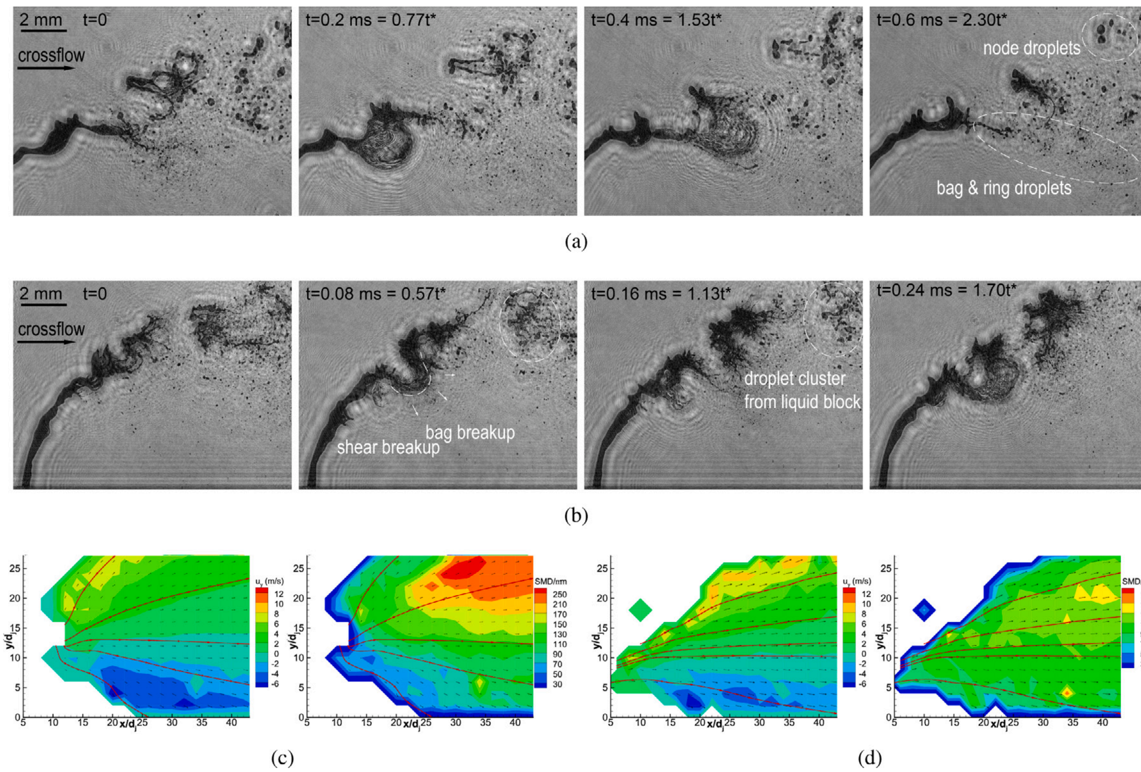

Fig. 4. Time resolved reconstructed images of bag breakup process of LJCF. z_r = 208 mm. (a) Case 2, $We_g = 11.0$, $q = 21.3$. (b) Case 6, $We_g = 41.0$, $q = 19.8$. (c) Transverse velocity and SMD distribution of Fig. 4(a) obtained through high speed holography. (d) Transverse velocity and SMD distribution of Fig. 4(b) obtained through high speed holography.

breakup region in LJCF. The aerodynamic force makes the sub-droplet cluster originating from bag breakup process generate a dispersed transverse velocity due to the pressure difference of the bag-shaped breakup. The SMD distribution indicates that droplet size are larger under case 2, that is because the knots and ligaments would be torn into smaller droplets under high We_g.

The liquid column breaking process is related to the upstream trajectory and downstream droplets distribution at the same time, so its position research is of importance. Wu [5] determined the breakup location as the distance from the nozzle exit to the column fracture point, but it is difficult to determine in actual LJCF cases because the bag membrane and ligaments interfere with the position determination of the end of the column. In this study, the liquid column position is determined using the down intersection of the first broken bag membrane and the liquid column. The breakup position and its standard deviation in each case were obtained from 50 different EFIs through image processing algorithm. Thereby, the relationship between the normalized breakup position and the We_g, q can be obtained, as is depicted in Fig. 5. The error bar in Fig. 5 is the standard deviation of the breakup position.

Under investigated cases, x_b/d_j varied from 5.0 to 10.2, and is approximately linear with We_g, and the fitting formula is $x_b/d_j = 11.2 - 0.143We_g$, with R-square of 0.91. y_b/d_j shows positive relationship with q and negative with We_g, with fitting formula of $y_b/d_j = 10.06We_g^{-0.348}q^{0.412}$ and R-square of 0.89. For the case in which the We_g is 67, shear breakup process along the liquid column near field is observed and the bag breakup position is not calculated. In the downstream of the liquid column breakup region, the node droplets are separated from the liquid column and the breakup time of these droplets is relatively long under low We_g, while under high We_g like $We_g = 36.4$, the node droplets interact with crossflow and break up into small drop cluster rapidly due to Rayleigh–Taylor instability. The breakup phenomenon leads to different distribution of the downstream droplet and will be discussed in the next section.

4.3. The 3D downstream droplet distribution

Thanks to the long depth of field characteristics of holography, most of the droplets can be displayed in focus on the image through the fusion extension process. Fig. 6 depicts EFIs and x - y projection SMD distributions of spray produced by the atomization of liquid jet in crossflow in four typical conditions. The spatial resolution of section is $3d_j \times 3d_j$. The SMD data is obtained through treatment of 100 holograms for each case, and the normalized droplet number contours map is drawn for each case. The trajectories are also drawn in these figures.

As is depicted in Fig. 6, the jet trajectory plotted by gray dots under $x/d_j < 10$ increases obviously with q, while the measured SMD region under $x/d_j > 10$ does not show such an obvious change. It is observed that the drop size distributions exhibit considerable differences under different We_g numbers. Under low Weber number, wave breakup process along the column jet generate large liquid knots one after another with troughs. These knots move in groups and gradually spread to the whole spray, and the velocity of large knots is hard to be changed by small aerodynamic force due to their large inertia, resulting in large SMD distribution at the outer periphery of spray, as are shown in Figs. 6(b) and 6(d). To be specific, small droplets originating from bag and ring breakup process are scattered throughout the near field of spray, but large knot droplets move in groups. As We_g rises to more than 36.5~42.4, a stronger drag force is exerted on the liquid column. According to [5,32], the breakup mode is converted from bag-like mode to multi-modal mode. Strong interaction between liquid knots and crossflow results in smaller SMD and more uniform size distribution. The SMD in the core region of the jet is relatively larger, indicating that larger droplets cannot penetrate farther under large We_g. As are shown in Figs. 6(f) and 6(h). The bag breakup process can be observed under all of the studied conditions, resulting in a lot of small droplets dispersed downstream, the ring droplets interact with crossflow and also break up into small droplets clusters thereby. The dispersion process may be affected by the wall counter

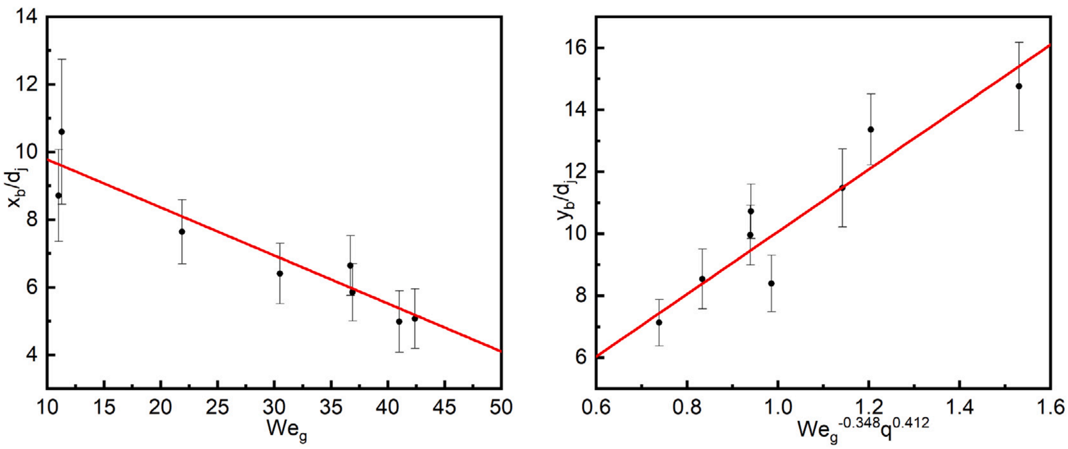

(a) (b)

Fig. 5. Nondimensional bag breakup position and fitting results of liquid jet. (a) x_b/d_j bag breakup position. (b) y_b/d_j bag breakup position.

vortex pair (CVP) near the wall and the upper CVP exists due to the interaction between the crossflow and liquid jet [33]. It is concluded by Ng [15] that $\mathrm{SMD_{bag}}/d_j \simeq 0.14$, $\mathrm{SMD_{ring}}/d_j \simeq 4.8We_g^{-1.0}$, and $\mathrm{SMD_{node}}/d_j \simeq 11.4We_g^{-1.0}$. The maximum SMD in Figs. 6(b) and 6(d) is close to 1, which approximates the node SMD fitting, while this value is slightly larger than the fit correlation under high We_g between 36.5~42.4. SMD distribution indicates that different types of droplets are mixed downstream. When q increases to about 20, it can be roughly considered that the droplets are mainly from the bag and ring breakup process in the area of $y < y_b$, and in the area of $y > y_b$, the droplets are mainly node droplets and small ones that further break up due to aerodynamic effects.

Fig. 7 depicts the normalized $y-z$ cross-section SMD and droplets sampling number distribution under $x/d_j = 70$, with spatial resolution of $3d_j \times 3d_j \times 3d_j$. The value shown on the solid line contours represents the sampling number of the droplets. More droplets are sampled in the core area of the spray. SMD in the core region is relative small due to weaker interaction between droplets and aerodynamic force than that around the spray plume. Node droplets result in higher SMD in the top region of the plume under a low We_g number. It is interesting to note that compared to the jet region depicted through SMD data, the jet trajectory obtained based on threshold segmentation method under $0 < x/d_j < 10$ from fused image underestimates the droplet dispersed area. This is because the concentration of droplets at the outer periphery of the jet plume is relatively low. Those droplets mostly come from the further breakup process of the node droplets, and the movement is the combination of jet motion and aerodynamic force during the breakup process. Small droplets in the upper and lower region of spray can be detected by PDPA or holography, but have a slight effect on the change of the gray value of the time average image [8], especially for far-field downstream of spray plume. To further quantify and characterize the influence of We_g and q on the downstream spray plume penetration, the volume flux distribution at an exact downstream slice can be calculated based on spatial droplet samples, and this parameter was mostly obtained with PDPA in previous studies [14,34]. Based on the volume flux distribution in the interval of $[x-\Delta x, x+\Delta x)$, the ratio k of the accumulated volume flux below a certain penetration depth y to the flow flux of the entire section can be obtained, which can be implemented by $k = \sum_{i, y_i \le y} d_i^3 / \sum_i d_i^3$, where y_i represents the penetration depth of droplet i. The ratio k is the function of the penetration depth y and the downstream distance x. The physical significance of this parameter is that for the spray plume downstream with many discrete droplets, it can be statistically known how deep the penetration depth is for the exact proportion of the volume flow. Consider the penetration depths where the k is closest to 50% and 90%, denoted as $y_{50\%}$ and $y_{90\%}$ respectively, and the normalized trajectory based on a limited number of statistical droplets along the x direction under different We and q can be obtained, which can be fitted by:

$$\frac{y_{90\%}}{d_j} = 3.470q^{0.410}We_g^{-0.067}\left(\frac{d_j}{d_0}\right)^{1.86}\left(\frac{x}{d_j}\right)^{0.441}, R^2 = 0.96, \mathrm{RSME} = 2.9; \tag{6}$$

$$\frac{y_{50\%}}{d_j} = 2.45q^{0.466}We_g^{-0.124}\left(\frac{d_j}{d_0}\right)^{1.90}\left(\frac{x}{d_j}\right)^{0.461}, R^2 = 0.95, \mathrm{RSME} = 2.4; \tag{7}$$

The fitting results depicted in Fig. 8 are valid under the conditions of $12 < x/d_j < 90, 10 < We_g < 67, 10 < q < 28$. From the fitting results of the downstream penetration depth, it can be observed that 90% volumetric flux trajectory is weakly correlated with We_g, which is similar to the fitting formula of the liquid column. The droplet size is relatively large in the core region of the spray plume under high We_g, as a result, the 50% volumetric flux trajectory has a certain negative correlation with the We_g. This correlation corroborates the phenomenon. The relatively large droplets cannot penetrate to the periphery of jet spray when the We_g is larger. Note that due to the blocking effect of the liquid membrane and the ligaments, it is hard to tell the 3D position and size information of the overlapped deformed droplets or ligaments in the optically dense region where the bag and shear breakup occurs [28,35], as a result, the prediction error of two formulas at the position where y/d_j is less than 15 (corresponding to the smaller x/d_j) is larger and could be more than 5.

5. Conclusion

In this article, liquid jets in a subsonic air crossflow have been characterized. Digital inline holography has been utilized to visualize the near field breakup modes as well as 3D droplet distributions downstream. The results lead to conclusions as follows:

- Picosecond pulsed digital inline holographic systems with a high speed of 25 kHz and a high resolution of 5.5 μm separately are established and are applied to obtain the bag-breakup process under a typical water jet in crossflow. This research obtained the trajectory of the liquid column, the position of the breakup point, and the downstream droplet distribution in the bag and multi-mode breakup regimes simultaneously.

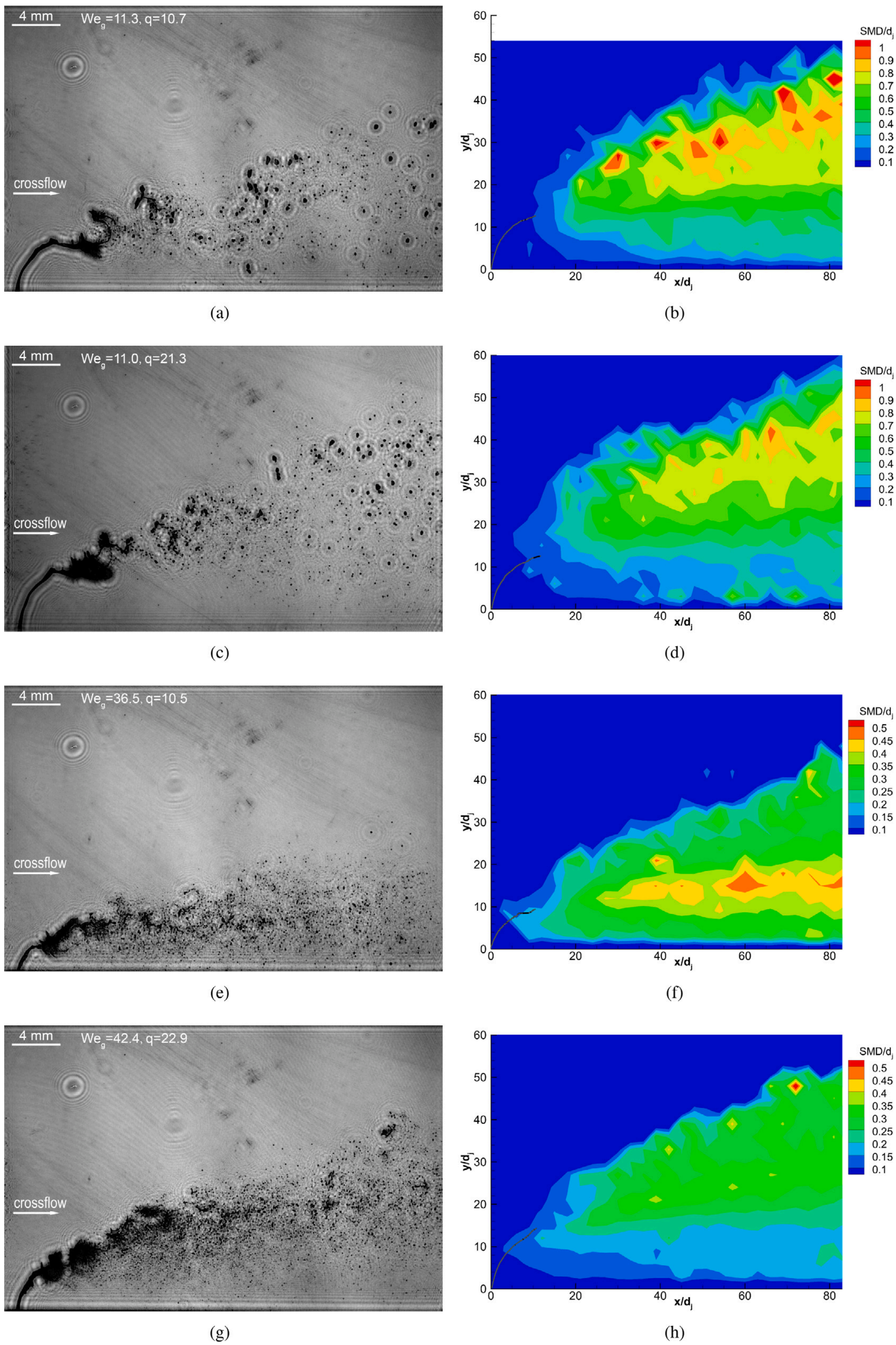

Fig. 6. Extended focus image of spray plume and corresponding $x-y$ slice SMD distribution under different cases. ((a)–(b)). Case 1. $We_g = 11.5$, $q = 10.7$. ((c)–(d)). Case 2. $We_g = 11.3$, $q = 21.3$. ((e)–(f)). Case 4. $We_g = 36.9$, $q = 10.5$. ((g)–(h)). Case 9. $We_g = 42.4$, $q = 22.9$.

- Regarding the jet tracking and liquid column breaking process, the jet trajectory under $0 < x/d_j < 10$ has a strong relationship with the momentum ratio q, but a weak relationship with the We number. This is consistent with previous studies and reviews [5].

Under the conditions studied, the bag breakup process is the main reason for the dispersion of fine droplets downstream of the jet. Based on the time-resolved results, in the area of $y < y_b$, droplets

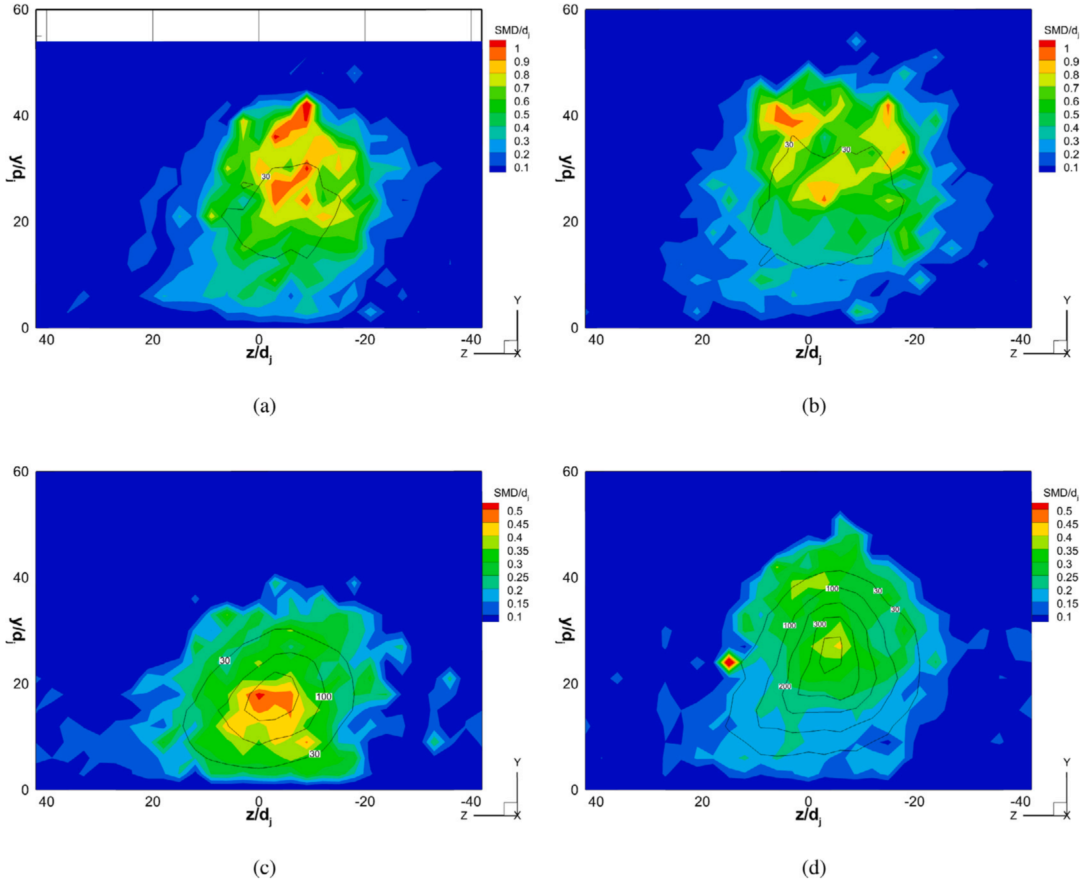

Fig. 7. The normalized $y-z$ slice SMD distribution and corresponding sampling droplet number distribution of LJCF under different cases, with $x/d_j = 70$. (a). Case 1 $We_g = 11.5$, $q = 10.7$. (b). Case 2. $We_g = 11.3$, $q = 21.3$. (c). Case 4. $We_g = 36.9$, $q = 10.5$. (d). Case 9. $We_g = 42.4$, $q = 22.9$.

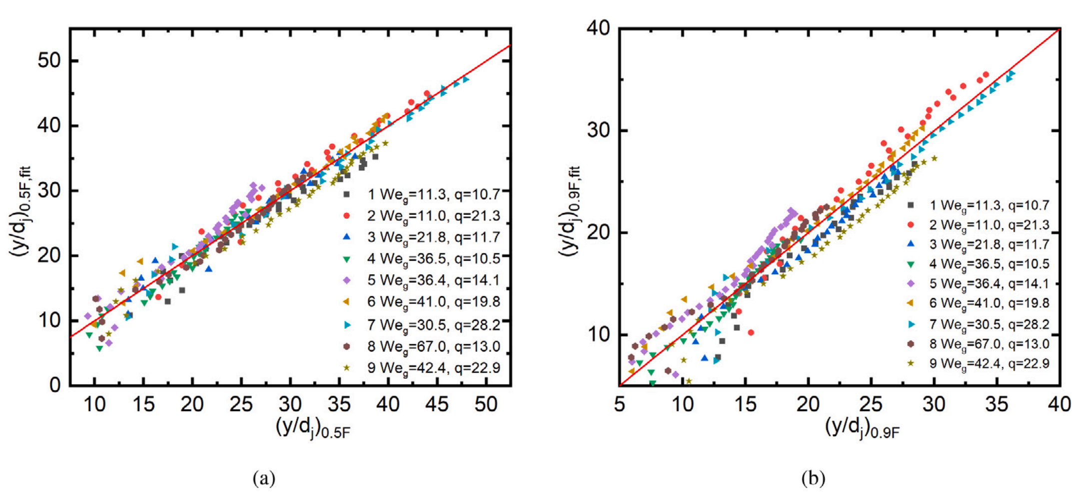

Fig. 8. Prediction and experiment results of nondimensional trajectory based on droplets volume flow. (a) 50% of the volume flow trajectory distribution. (b) 90% of the volume flow trajectory distribution.

with negative transverse velocity are mainly from the bag and ring breakup process.

- Combining the jet trajectory and the downstream particle size distribution, it can be found that q mainly influence the particle size distribution range of the downstream droplets, while We_g mainly changes the dispersion region of large-size droplets in the spray plume. The discussion is supported by both the $x-y$ projected SMD distribution and $y-z$ cross-section SMD distribution calculated from the holograms.
- The 3D droplets distributions under $x/d_j < 90$ downstream of the LJCF are obtained based on holographic treat algorithm. The downstream spray plume penetrations are also obtained based on the volume flow, which can avoid the recognition error of spray edge facing sparse droplets and complex background intensity. In addition, the fitted penetration formulas under different volume flow ratios also show the influence of the We_g number on the droplet spatial distribution.

CRediT authorship contribution statement

Lei Wang: Writing – original draft, Software, Writing – review & editing, Data curation, Methodology, Investigation. **Letian Zhang:** Visualization, Investigation, Writing – original draft, Software, Writing – review & editing. **Wenhui Lin:** Investigation, Data curation, Writing – original draft. **Yingchun Wu:** Conceptualization, Supervision, Software, Writing – review & editing, Funding acquisition. **Xuecheng Wu:** Resources, Conceptualization, Project administration, Funding acquisition.

Declaration of competing interest

The authors declare that they have no known competing financial interests or personal relationships that could have appeared to influence the work reported in this paper.

Data availability

Data will be made available on request.

Acknowledgments

The authors gratefully acknowledge the support from National Science and Technology Major Project (J2019-III-0006-0049).

References

[1] J. Mazallon, Z. Dai, G. Faeth, Primary breakup of nonturbulent round liquid jets in gas crossflows, At. Spray. 9 (3) (1999) 291–312.
[2] R. Suryaprakash, G. Tomar, Secondary breakup of drops, J. Indian Inst. Sci. 99 (1) (2019) 77–91.
[3] M. Broumand, M. Birouk, Liquid jet in a subsonic gaseous crossflow: recent progress and remaining challenges, Prog. Energy Sci. Combust. 57 (2016) 1–29.
[4] A. Jones, M. Sarjeant, C. Davis, R. Denham, Application of in-line holography to drop size measurement in dense fuel sprays, Appl. Opt. 17 (3) (1978) 328_1–330.
[5] P.-K. Wu, K.A. Kirkendall, R.P. Fuller, A.S. Nejad, Breakup processes of liquid jets in subsonic crossflows, J. Propul. Power 13 (1) (1997) 64–73.
[6] S.-Y. No, A review on empirical correlations for jet/spray trajectory of liquid jet in uniform cross flow, Int. J. Spray Combust. Dyn. 7 (4) (2015) 283–313.
[7] M. Wang, M. Broumand, M. Birouk, Liquid jet trajectory in a subsonic gaseous cross-flow: an analysis of published correlations, At. Spray. 26 (11) (2016) 1083–1110.
[8] A. Amighi, N. Ashgriz, Trajectory of a liquid jet in a high temperature and pressure gaseous cross flow, J. Eng. Gas Turbines Power 141 (6) (2019).
[9] M. Broumand, M.M. Ahmed, M. Birouk, Experimental investigation of spray characteristics of a liquid jet in a turbulent subsonic gaseous crossflow, Proc. Combust. Inst. 37 (3) (2019) 3237–3244.
[10] G. Olyaei, A. Kebriaee, Experimental study of liquid jets injected in crossflow, Exp. Therm. Sci. Fluids 115 (2020) 110049.
[11] R.S. Prakash, A. Sinha, G. Tomar, R. Ravikrishna, Liquid jet in crossflow–effect of liquid entry conditions, Exp. Therm. Sci. Fluids 93 (2018) 45–56.
[12] Y. Song, D. Hwang, K. Ahn, Effect of orifice geometry on column trajectories of liquid jets in crossflows, Int. J. Aeronaut. Space Sci. 20 (1) (2019) 139–149.
[13] K. Sallam, C. Aalburg, G. Faeth, Breakup of round nonturbulent liquid jets in gaseous crossflow, AIAA J. 42 (12) (2004) 2529–2540.
[14] P.-K. Wu, K.A. Kirkendall, R.P. Fuller, A.S. Nejad,
[15] C.L. Ng, R. Sankarakrishnan, K.A. Sallam, Bag breakup of nonturbulent liquid jets in crossflow, Int. J. Multiph. Flow. 34 (3) (2008) 241–259.
[16] T. Inamura, N. Nagai, Spray characteristics of liquid jet traversing subsonic airstreams, J. Propul. Power 13 (2) (1997) 250–256.
[17] E. Lubarsky, J.R. Reichel, B.T. Zinn, R. McAmis, Spray in crossflow: dependence on Weber number, J. Eng. Gas Turbines Power 132 (2) (2010) 021501.
[18] E. Lubarsky, D. Shcherbik, O. Bibik, Y. Gopala, B. Zinn, Fuel jet in cross flow—experimental study of spray characteristics, Adv. Fluid Dyn. (2012) 59.
[19] K.D. Kihm, G.M. Lyn, S.Y. Son, Atomization of cross-injecting sprays into convective air stream, At. Spray. 5 (4–5) (1995) 417–433.
[20] J. Song, C.C. Cain, J.G. Lee, Liquid jets in subsonic air crossflow at elevated pressure, in: ASME Turbo Expo 2014: Turbine Technical Conference and Exposition, Vol. 4B: Combustion, Fuels and Emissions, V04BT04A018.
[21] J. Katz, J. Sheng, Applications of holography in fluid mechanics and particle dynamics, Annu. Rev. Fluid Mech. 42 (1) (2010) 531–555.
[22] D.R. Guildenbecher, L. Engvall, J. Gao, T.W. Grasser, P.L. Reu, J. Chen, Digital in-line holography to quantify secondary droplets from the impact of a single drop on a thin film, Exp. Fluids 55 (3) (2014) 1670.
[23] D.R. Guildenbecher, J. Gao, J. Chen, P.E. Sojka, Characterization of drop aerodynamic fragmentation in the bag and sheet-thinning regimes by crossed-beam, two-view, digital in-line holography, Int. J. Multiph. Flow. 94 (2017) 107–122.
[24] B. Lebon, G. Perret, S. Cotmellec, G. Godard, G. Gréhan, D. Lebrun, J. Brossard, A digital holography set-up for 3d vortex flow dynamics, Exp. Fluids 57 (6) (2016) 103.
[25] Y. Wu, L. Wang, W. Lin, G. Song, Y. He, X. Wu, Z. Wang, K. Cen, Picosecond pulsed digital off-axis holography for near-nozzle droplet size and 3d distribution measurement of a swirl kerosene spray, Fuel 283 (2021) 119124.
[26] L. Yao, X. Wu, Y. Wu, J. Yang, X. Gao, L. Chen, G. Gréhan, K. Cen, Characterization of atomization and breakup of acoustically levitated drops with digital holography, Appl. Opt. 54 (1) (2015) A23–A31.
[27] L. Yao, J. Chen, P.E. Sojka, X. Wu, Characterization of the bag breakup of liquid drop using high-speed digital in-line holography, in: Fluids Engineering Division Summer Meeting, Vol. 51562, American Society of Mechanical Engineers, 2018, V002T14A015.
[28] D. Olinger, K. Sallam, K.-C. Lin, C. Carter, Digital holographic analysis of the near field of aerated-liquid jets in crossflow, J. Propul. Power 30 (6) (2014) 1636–1645.
[29] W. Yingchun, W. Xuecheng, Y. Jing, W. Zhihua, G. Xiang, Z. Binwu, C. Linghong, Q. Kunzan, G. Gréhan, C. Kefa, Wavelet-based depth-of-field extension, accurate autofocusing, and particle pairing for digital inline particle holography, Appl. Opt. 53 (4) (2014) 556–564.
[30] A. Mashayek, A. Jafari, N. Ashgriz, Improved model for the penetration of liquid jets in subsonic crossflows, AIAA J. 46 (11) (2008) 2674–2686.
[31] J. Nicholls, A. Ranger, Aerodynamic shattering of liquid drops, AIAA J. 7 (2) (1969) 285–290.
[32] K.A. Sallam, C. Aalburg, G.M. Faeth, K.C. Lin, C.D. Carter, T.A. Jackson, Primary breakup of round aerated-liquid jets in supersonic crossflows, At. Spray. 16 (6) (2006) 657–672.
[33] J. Chang, Y. Du, X. Shao, Y. Zhao, S. Zheng, Investigation and analysis of vortex and application of jet in crossflow, Case Stud. Therm. Eng. 14 (2019) 100459.
[34] J. Becker, C. Hassa, Breakup and atomization of a kerosene jet in crossflowat elevated pressure, At. Spray. 12 (1–3) (2002) 49–67.
[35] D. Olinger, K. Sallam, K.-C. Lin, C. Carter, Digital holographic analysis of near-field aerated liquid jets in crossflow, part II: measurements, in: 51st AIAA Aerospace Sciences Meeting Including the New Horizons Forum and Aerospace Exposition, 2013, p. 167.